JRC Scientific and Technical Reports

Grain boundary modeling issues with cohesive elements: application to intergranular stress corrosion cracking.

Igor Simonovski, Gangadhar Machina

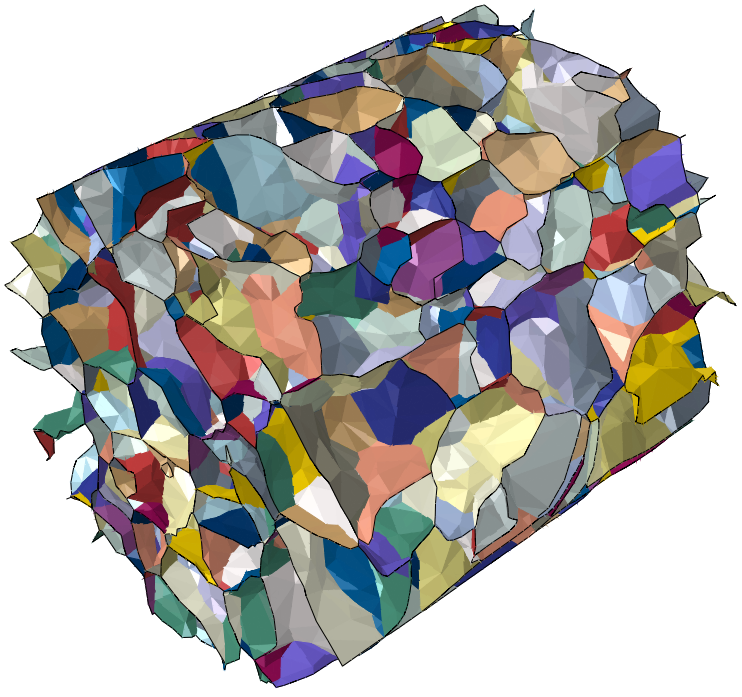

EUR 25144 EN - 2012

JRC EUROPEAN COMMISSION

Institute for Energy and Transport

The mission of the JRC-IET is to provide support to Community policies related to both nuclear and non-nuclear energy in order to ensure sustainable, secure and efficient energy production, distribution and use.

European Commission
Joint Research Centre
Institute for Energy and Transport

Contact information
Address: Safety of Present Nuclear Reactors Unit, P.O. Box 2, NL-1755 ZG Petten, The Netherlands
E-mail: Igor.Simonovski@ec.europa.eu
Tel.: + 31 (0)224 56 5072
Fax: + 31 (0)224 56 5641

http://ie.jrc.ec.europa.eu/
http://www.jrc.ec.europa.eu/

JRC 68140
EUR 25144 EN

ISBN 978-92-79-22608-3 (pdf)
ISBN 978-92-79-22607-6 (print)
ISSN 1831-9424 (online)
ISSN 1018-5593 (print)
doi http://dx.doi.org/10.2790/40327

Luxembourg: Publications Office of the European Union

Printed in The Netherlands

Contents

Chapter 1

Introduction

Stress corrosion cracking (SCC) is a process of crack initiation and subcritical crack growth of susceptible alloys in corrosive environment under the influence of tensile stress or strain [1]. SCC can manifest itself as intergranular (along the grain boundaries), transgranular (through the grains) cracks or can include both types of cracks. The first form is referred to as intergranular stress corrosion cracking (IGSCC) while the second type as transgranular stress corrosion cracking (TGSCC). SCC has been detected in sensitized stainless steels (SS) as early as 1961, afterwards in SS weld piping in 1970s and in boiling water reactor (BWR) internals during 1980s. It has been observed in a variety of materials (e.g. Ni-based alloys, 304L, 316L, SA 453 Grade 660) and components (e.g. steam generator tubes, pressurizer sleeves, control road drive mechanism penetration nozzles, welds and steam generator divider plates).

SCC can importantly contribute to degradation of components in nuclear power plants. For example, a leak in the penetration to the pressure vessel head, caused by SCC, was discovered in 1991 at the Bugey 3 Nuclear Power plant in France. The main crack initiated in Alloy 600 base metal and propagated into the Alloy 182 weld metal [2]. In the U.S. the through wall cracking was found in three control rod drive mechanism (CRDM) nozzles at Davis-Besse Nuclear Power Station in 2002 [3].

The basic SCC degradation mechanism initiates at a very small scales. At these scales the microstructure of the material plays a significant role. This role is still not fully understood. In recent years we have observed the advent of new experimental techniques such as differential aperture X-ray microscopy [4], 3D X-ray diffraction microscopy (3DXRD) [5] and X-ray diffraction contrast tomography (DCT) [6, 7]. Through these techniques grain shapes and orientations can be measured non-destructively and even crack initiation and growth can be monitored [8]. These techniques can be combined with advanced grain-level models to better understand the damage mechanisms and the role of the microstructure. Finite element (FE) modeling approach is extensively used for developing grain-level models of microstructure. Researchers are now able to reconstruct as-measured steel structure in a finite element model [9, 10, 11]. Several issues like for example constitutive behavior of bulk grains and grain boundaries are, however, still being investigated. One approach for modeling grain boundaries is cohesive zone approach where the grain boundary is modeled using traction-separation response. However, there are certain issues relating to the accuracy and performance of these elements. This work documents these issues and presents them in the context of grain-level finite element models of microstructure. Both analytical and as-measured microstructures are employed.

Chapter 2

Cohesive zone approach for grain boundaries

Experimental observations [12] show that a cohesive-zone approach [13] is an appropriate way of modeling the grain boundary constitutive response. In FE method the cohesive-zone approach is typically implemented by using cohesive-zone elements. Since a grain boundary thickness is significantly smaller compared to the grain size, zero-thickness cohesive elements can be used. For very thin and zero-thickness layers cohesive elements based upon a traction-separation response are recommended [14]. A typical traction-separation response of such an element is shown in Fig. 2.1.

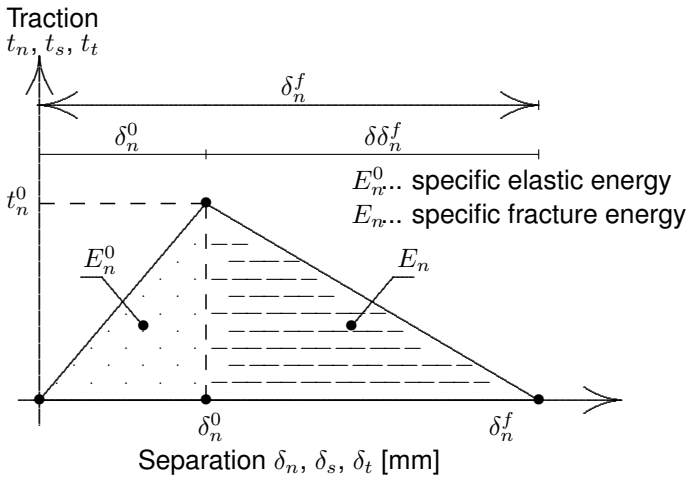

Figure 2.1: Example of traction-separation response (not to scale).

The strains ϵ in the cohesive elements are defined using the constitutive thickness of the cohesive element T_0 (mostly different from the geometric thickness which is typically close or equal to zero) and the separations of the element nodes δ as compared to their initial unloaded positions, Eq. (2.1).

$$\left\{ \begin{array}{c} \epsilon_n \\ \epsilon_s \\ \epsilon_t \end{array} \right\} = \frac{1}{T_0} \left\{ \begin{array}{c} \delta_n \\ \delta_s \\ \delta_t \end{array} \right\} \tag{2.1}$$

The indices n, s and t denote the normal and two orthogonal shear directions of the cohesive element. The normal direction always points out of the plane of the cohesive element. The tractions on the cohesive elements are then given by Eq. (2.2).

$$\left\{ \begin{array}{c} t_n \\ t_s \\ t_t \end{array} \right\} = \left[\begin{array}{ccc} K_{nn} \cdot D(\delta) & 0 & 0 \\ 0 & K_{ss} \cdot D(\delta) & 0 \\ 0 & 0 & K_{tt} \cdot D(\delta) \end{array} \right] \left\{ \begin{array}{c} \epsilon_n \\ \epsilon_s \\ \epsilon_t \end{array} \right\} \tag{2.2}$$

where $D(\delta)$ stands for damage evolution, defined by Eq. (2.3) for the normal direction (and both shear directions).

$$D(\delta) = \left\{ \begin{array}{ll} 0 & ; \quad \delta < \delta_n^0 \\ \frac{\delta_n^f \left(\delta - \delta_n^0\right)}{\delta \left(\delta_n^f - \delta_n^0\right)} & ; \quad \delta \geq \delta_n^0 \end{array} \right\} \tag{2.3}$$

The actual load-carrying capability of the cohesive element in the normal direction would then be $[1 - D(\delta)]\, K_{nn}$ and correspondingly for the two shear directions. Various damage evolution laws can be used, however, due to simplicity the damage evolution resulting in linear stiffness decrease, Eq. (2.3), is used in this work.

Chapter 3

Cohesive elements issues

3.1 Stresses in the normal direction

In this section we explore the response of the cohesive elements in their normal direction. A normal direction is defined as a through-thickness direction and is perpendicular to the element's main faces (Face 1 and Face 2), see Fig. 3.1.

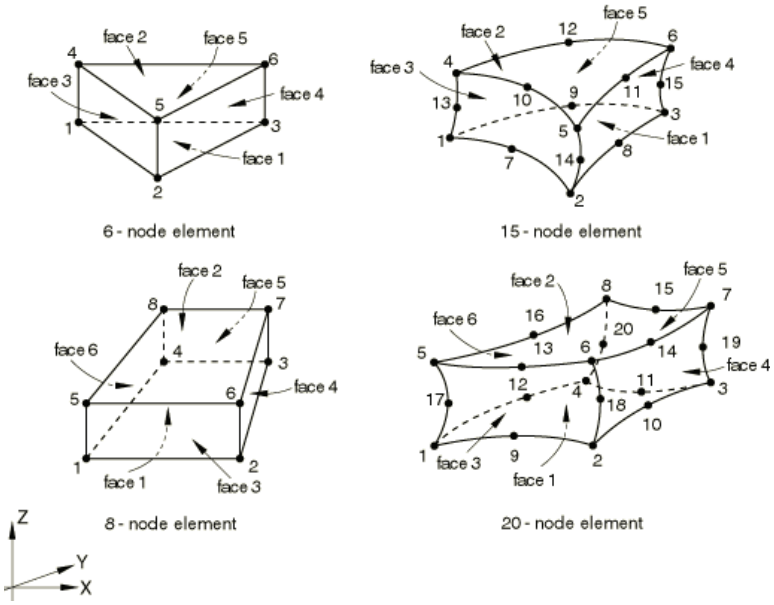

Figure 3.1: Faces of the cohesive elements [14].

Given the stress tensor σ_{ij} a stress vector p_i on a given plane n_j is defined by Eq. (3.1).

$$p_i = \sigma_{ij} \cdot n_j \tag{3.1}$$

Normal stress σ_n on the same plane n_j is then given by Eq. (3.2).

$$\sigma_n = p_i \cdot n_i \tag{3.2}$$

Therefore, if the stress tensor within the cohesive element is known, we can compute the normal stress as we know the planes($\equiv$ faces) of the cohesive element.

3.1.1 Simple 3D Y model

Let us have a cuboid, divided into three grains as depicted in the Fig. 3.2 by the three colors. Let us put 100 MPa of tensile stress on the top and the bottom surface and 200 MPa of tensile stress on the left and right surface. Let

us constrain the front and the back surface in the Z direction, resulting in ϵ_{33}=0. Furthermore, let us assume that we are dealing with homogeneous, isotropic elastic material with Young modulus E=200 000 MPa and Poisson ratio of ν=0.3. For a homogeneous, isotropic elastic material Eqs. (3.3,3.4) relate the strains to the stresses.

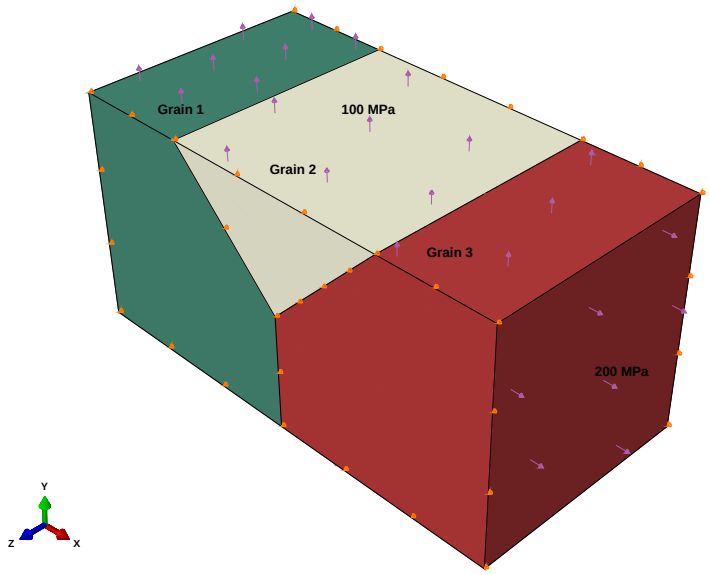

Figure 3.2: A simple Y model.

$$\sigma_{11} = \frac{E}{1+\nu}\epsilon_{11} + \frac{E\nu}{(1+\nu)(1-2\nu)}(\epsilon_{11}+\epsilon_{22}+\epsilon_{33}) \tag{3.3}$$

$$\sigma_{22} = \frac{E}{1+\nu}\epsilon_{22} + \frac{E\nu}{(1+\nu)(1-2\nu)}(\epsilon_{11}+\epsilon_{22}+\epsilon_{33}) \tag{3.4}$$

$$\sigma_{33} = \frac{E}{1+\nu}\epsilon_{33} + \frac{E\nu}{(1+\nu)(1-2\nu)}(\epsilon_{11}+\epsilon_{22}+\epsilon_{33}) \tag{3.5}$$

From Eqs. (3.3,3.4), expressions Eqs. (3.6,3.7) can be derived as ϵ_{33}=0 due to the boundary conditions. Using σ_{11}=200 MPa and σ_{22}=100 MPa we obtain values $\epsilon_{22} = 6.5 \cdot 10^{-5}$ and $\epsilon_{11} = 7.15 \cdot 10^{-4}$. Inserting these two values in Eq. (3.5) we obtain σ_{33}=90 MPa.

$$\epsilon_{22} = \frac{\sigma_{11}(1+\nu)(1-2\nu) - \sigma_{22}\frac{(1+\nu)(1-2\nu)(1-\nu)}{\nu}}{E\nu - E\frac{(1-\nu)^2}{\nu}} \tag{3.6}$$

$$\epsilon_{11} = \frac{\sigma_{22}(1+\nu)(1-2\nu) - \epsilon_{22}E(1-\nu)}{E\nu} \tag{3.7}$$

The resulting stress tensor is given by Eq. (3.8).

$$\sigma_{ij} = \begin{bmatrix} 200 & 0 & 0 \\ 0 & 100 & 0 \\ 0 & 0 & 90 \end{bmatrix} \text{MPa} \tag{3.8}$$

The boundaries between the grain are defined with the vectors, normal to the planes of the grain boundaries.

$$n_{Grain_1 Grain_2} = \pm \begin{bmatrix} 1 \\ 1 \\ 0 \end{bmatrix} \cdot \frac{1}{\sqrt{2}} \tag{3.9}$$

$$n_{Grain_2 Grain_3} = \pm \begin{bmatrix} -1 \\ 1 \\ 0 \end{bmatrix} \cdot \frac{1}{\sqrt{2}} \tag{3.10}$$

$$n_{Grain_1Grain_3} = \pm \begin{bmatrix} 1 \\ 0 \\ 0 \end{bmatrix} \cdot \frac{1}{\sqrt{2}} \tag{3.11}$$

Since we know the stress tensor and the normals for these three planes, we can compute the stresses in the normal direction for each of them. For the plane between the $Grain_1$ and $Grain_2$ the stress vector on the plane, p, and the normal stress, σ_n, are given by Eq. (3.12) and Eq. (3.13).

$$Grain_1Grain_2: \quad p = \begin{bmatrix} 200 & 0 & 0 \\ 0 & 100 & 0 \\ 0 & 0 & 90 \end{bmatrix} \cdot (\pm) \begin{bmatrix} 1 \\ 1 \\ 0 \end{bmatrix} \cdot \frac{1}{\sqrt{2}} = \pm \begin{bmatrix} 200 \\ 100 \\ 0 \end{bmatrix} \cdot \frac{1}{\sqrt{2}} \,\text{MPa} \tag{3.12}$$

$$Grain_1Grain_2: \quad \sigma_n = p_i \cdot n_i = 150\,\text{MPa} \tag{3.13}$$

Similarly, we obtain the following normal stress values for the other two planes:

$$Grain_2Grain_3: \quad \sigma_n = 150\,\text{MPa} \tag{3.14}$$

$$Grain_1Grain_3: \quad \sigma_n = 200\,\text{MPa} \tag{3.15}$$

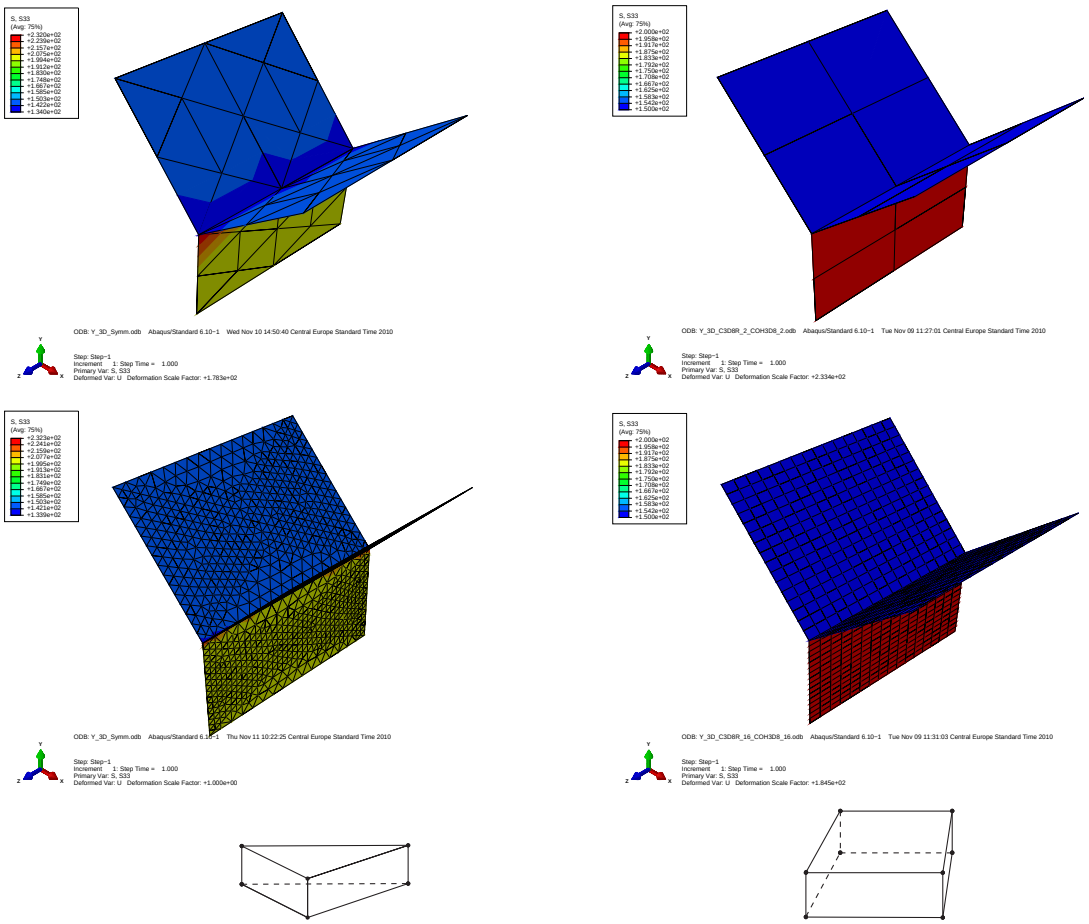

Figure 3.3: Normal stresses in the cohesive elements. Triangular prisms (left) and rectangular prisms (right) cohesive elements. Variation in stress at the Y triple points can be observed for the triangular prism cohesive elements. Bottom row indicates the type of the cohesive element.

Fig. 3.3 displays the normal stresses in the cohesive elements as calculated from the ABAQUS FE models. The physical thickness of the cohesive elements is zero. On the left hand side triangular prism cohesive elements are used, whereas on the right hand side rectangular prism cohesive elements are used. One can see that in the case of triangular prisms there is a variation in the normal stress for a given plane, in particular at the Y triple points. For the rectangular prism cohesive elements no such variations are observed and the values from the FE model match exactly with the theoretically computed values.

Symmetric geometries, symmetric meshes

In this section the effect of different meshes on the computed normal stresses is presented. The geometry is the same as in Fig. 3.2, with no surface partitioning, see Fig. 3.4. Tables 3.1, 3.2, 3.3 and 3.4 show the corresponding results. One can see that:

1. Only a conformal mesh with hexahedra cohesive elements results in constant normal stresses on the grain boundaries.
2. Prism cohesive elements result in deviations from the theoretical normal stresses at the triple line between the three grains.
   (a) Increasing the mesh density alleviates the problem to a certain extent.
   (b) Non-conformal mesh exacerbates the problem.

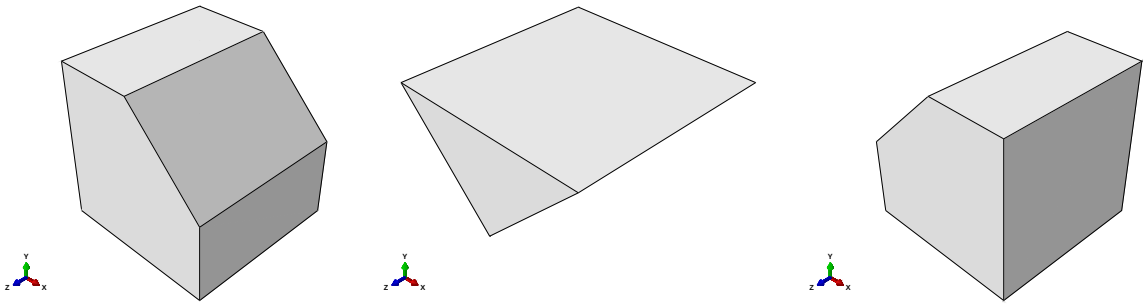

Grain 1 Grain 2 Grain 3

Figure 3.4: Grain geometry with no surface partitioning.

Symmetric geometries, mostly symmetric meshes

In this section the basic geometry is the same as in Fig. 3.2, however, surface partitioning is introduced to the grains, see Fig. 3.5. The effect of surface partitioning is important since a real steel structure contains extremely complex grain shapes whose surfaces are reconstructed with triangles in 3D space, see Fig. 3.6. Table 3.5 shows the corresponding results.

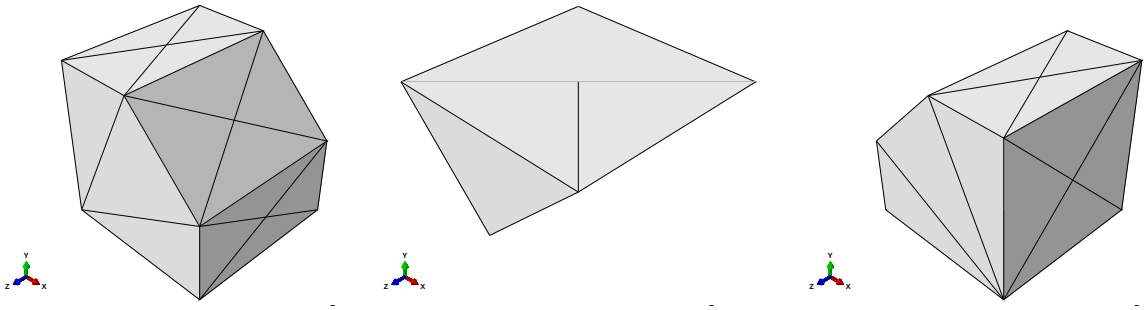

Grain 1 Grain 2 Grain 3

Figure 3.5: Grain geometry with surface partitioning.

Comparing the results to the the ones in the Table 3.3 where the same mesh density is used with the same structural and cohesive elements, one can see that:

1. Surface partitioning results in larger deviations at the same mesh density.
2. Increasing the mesh density alleviates the problem to a certain extent.

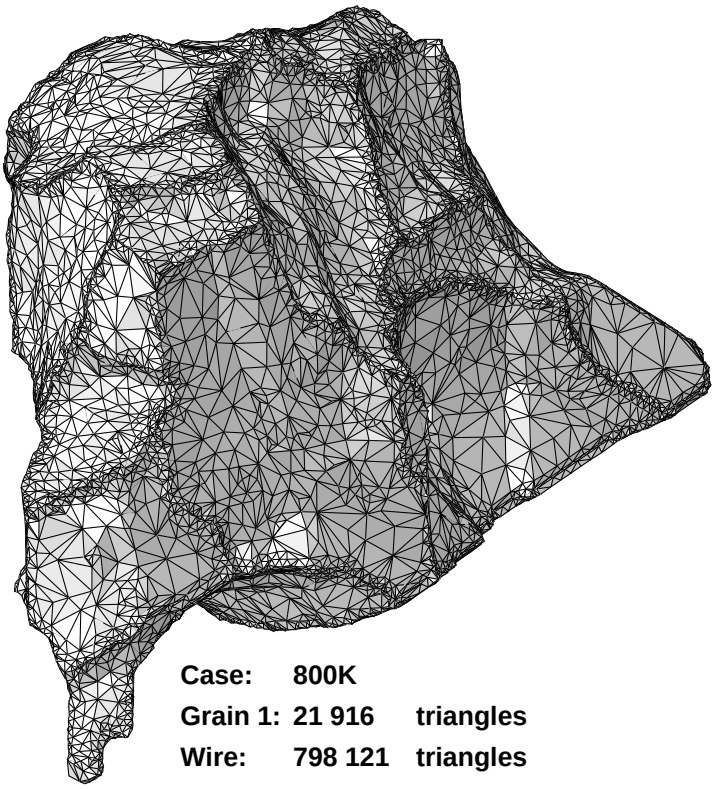

Figure 3.6: An example of a measured grain shape.

Non-conformal mesh comparison

Once the damage initializes in the cohesive elements, the size of cohesive elements begins to plays a significant role. A process zone (often called also a cohesive zone) develops in front of the crack. To be able to capture the crack evolution properly, the cohesive elements should be smaller than the process zone [15]. For a constant failure stress the process zone length is given by Eq. (3.16) [16]. On the other hand, when the failure stress varies linearly within the cohesive zone, the process zone length is given by Eq. (3.17) [17].

$$\alpha = \frac{\pi}{8}\left(\frac{K_I}{t_n^0}\right)^2 \tag{3.16}$$

$$\alpha = \frac{9\pi}{32}\left(\frac{K_I}{t_n^0}\right)^2 \tag{3.17}$$

If we use K_{Ic}=50 MPa m$^{\frac{1}{2}}$ and t_n^0=205 MPa, Eq. (3.16) results in a requirement that the cohesive element size is smaller than α=2.3E-2 μm. This is an extremely small element size which results in an enormous number of finite elements if a conformal mesh is used. A denser mesh of the cohesive layer compared to the surrounding bulk grain mesh would be preferred. This is also recommended by [14]. However, we have already seen that a non-conformal mesh results in higher deviations from the theoretical normal stresses at the triple lines between the grains, see Tables 3.2 and 3.4.

Table 3.1: Comparison of hexahedra structural and cohesive element combinations: **CONFORMAL MESHES**.

Structural elements		Cohesive elements		Grain mesh	Cohesive S33 values
Element type	Elements per edge	Element type	Elements per edge		
C3D8R	2	COH3D8	2	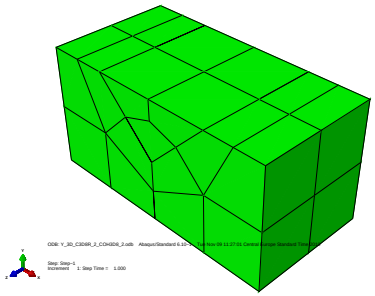	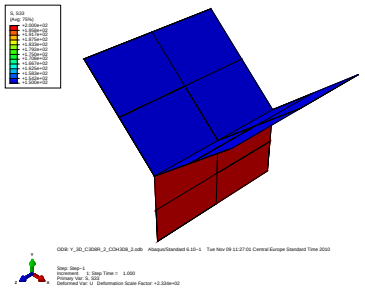
C3D8R	4	COH3D8	4	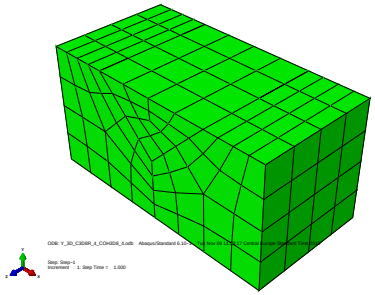	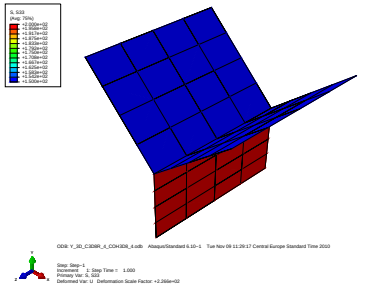
C3D8R	8	COH3D8	8	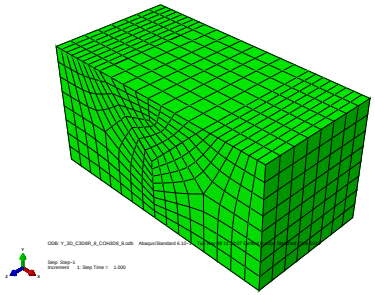	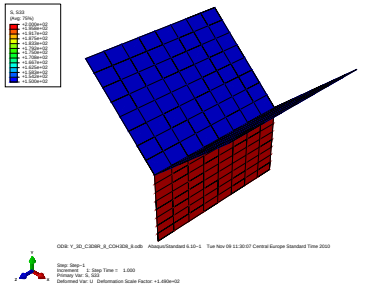
C3D8R	16	COH3D8	16	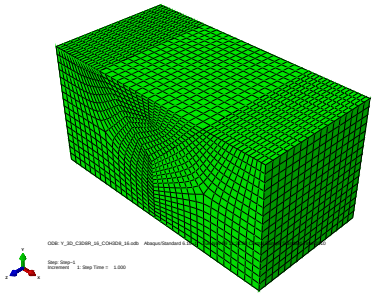	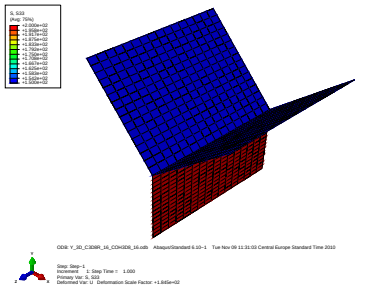

Table 3.2: Comparison of hexahedra structural and cohesive element combinations: **NON-CONFORMAL MESHES**.

Structural elements		Cohesive elements		Grain mesh	Cohesive S33 values
Element type	Elements per edge	Element type	Elements per edge		
C3D8R	2	COH3D8	2	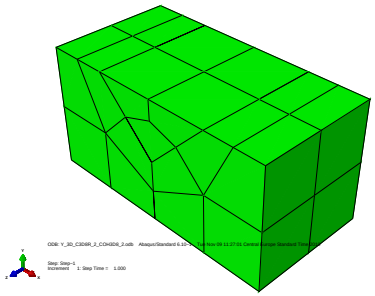	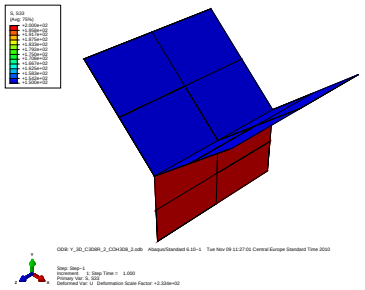
C3D8R	2	COH3D8	4	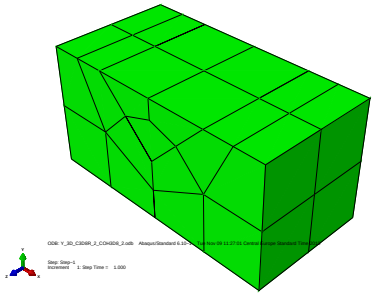	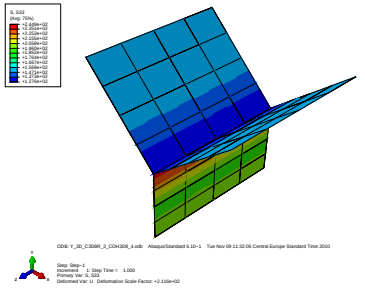
C3D8R	2	COH3D8	8	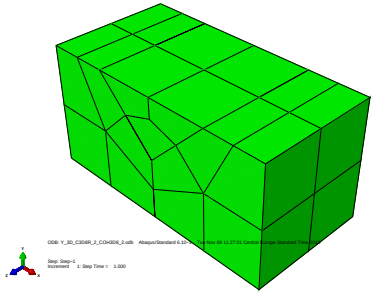	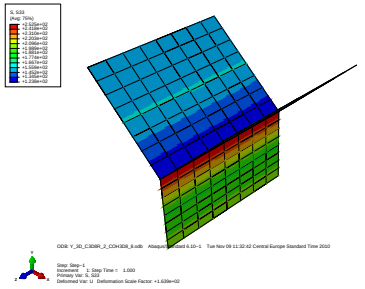
C3D8R	2	COH3D8	16	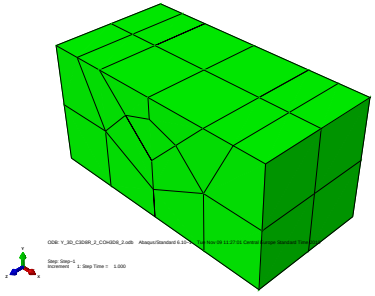	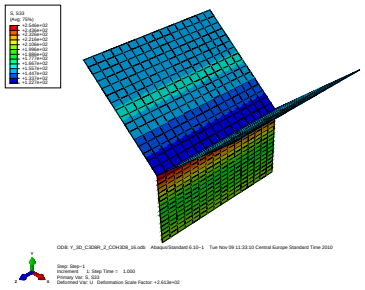

Table 3.3: Comparison of tetrahedra structural and prism cohesive element combinations: **CONFORMAL MESHES**.

Structural elements		Cohesive elements		Grain mesh	Cohesive S33 values
Element type	Elements per edge	Element type	Elements per edge		
C3D4	2	COH3D6	2	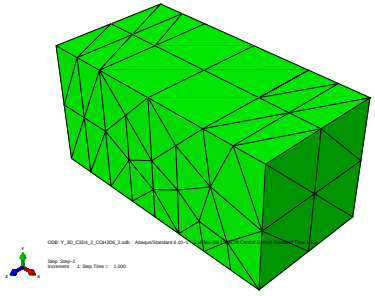	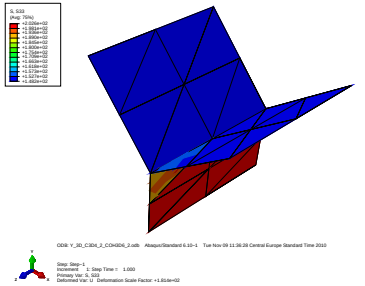
C3D4	4	COH3D6	4	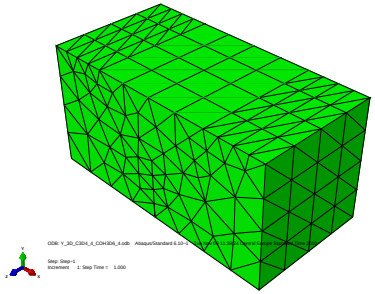	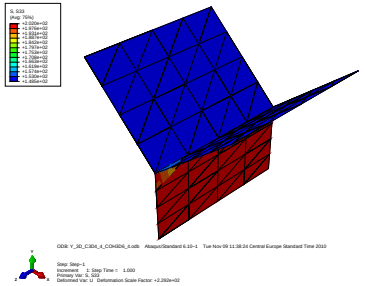
C3D4	8	COH3D6	8	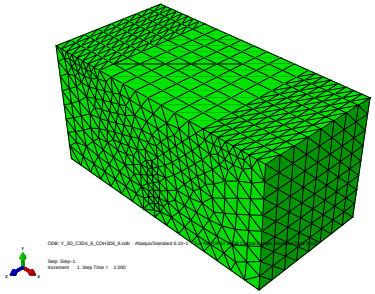	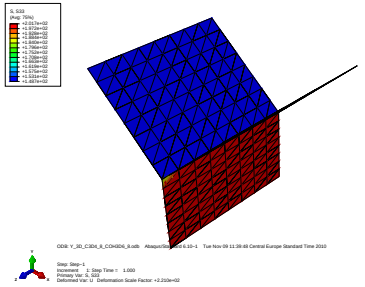
C3D4	16	COH3D6	16	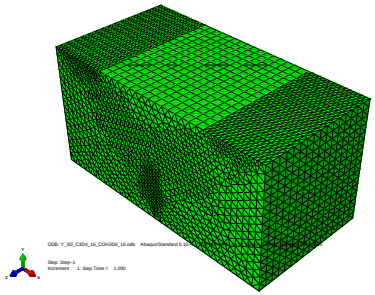	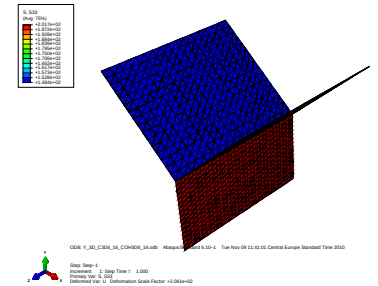

Table 3.4: Comparison of tetrahedra structural and prism cohesive element combinations: **NON-CONFORMAL MESHES**.

Structural elements		Cohesive elements		Grain mesh	Cohesive S33 values
Element type	Elements per edge	Element type	Elements per edge		
C3D4	2	COH3D6	2	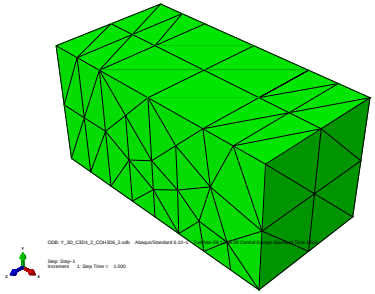	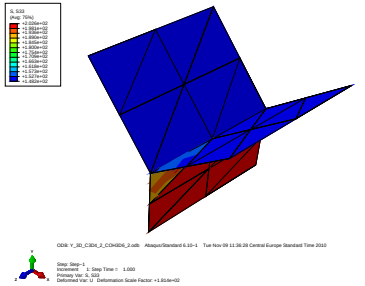
C3D4	2	COH3D6	4	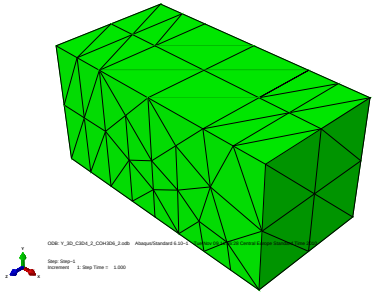	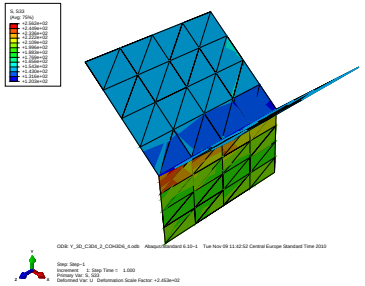
C3D4	2	COH3D6	8	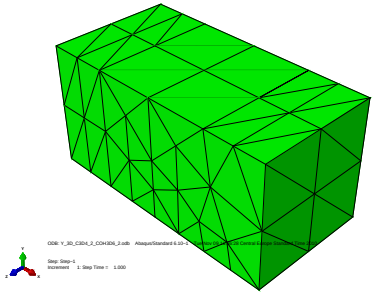	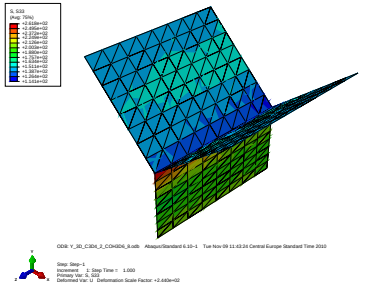
C3D4	2	COH3D6	16	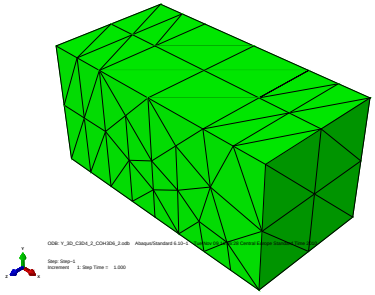	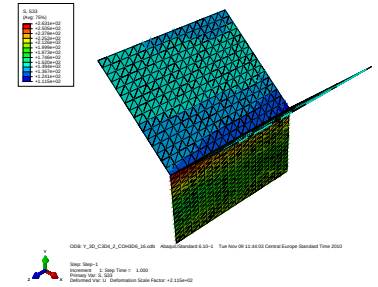

Table 3.5: Comparison of tetrahedra structural and prism cohesive element combinations: **CONFORMAL MESHES**

Structural elements		Cohesive elements		Grain mesh	Cohesive S33 values
Element type	Elements per edge	Element type	Elements per edge		
C3D4	2	COH3D6	2	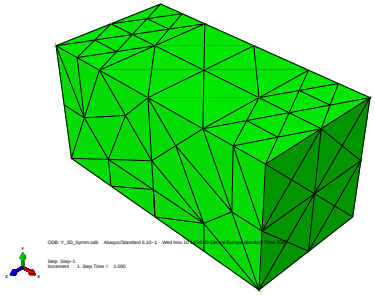	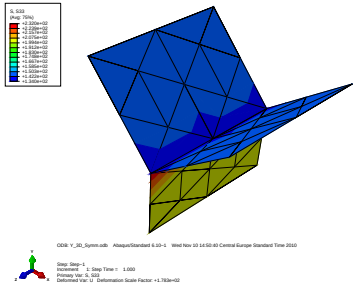
C3D4	4	COH3D6	4	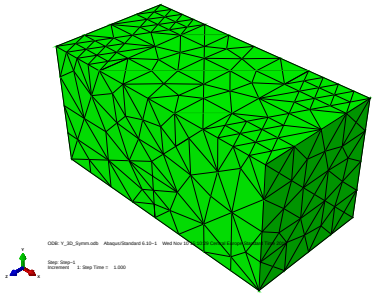	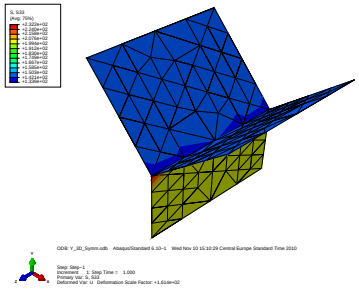
C3D4	8	COH3D6	8	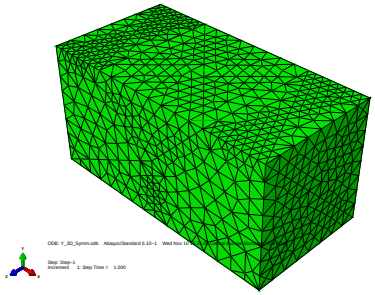	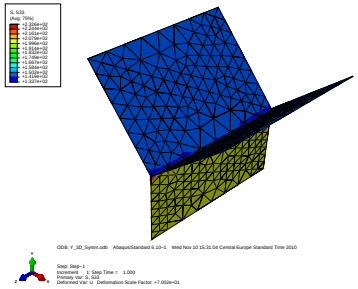
C3D4	16	COH3D6	16	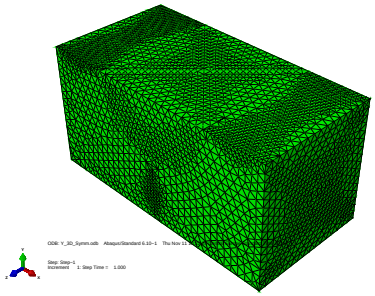	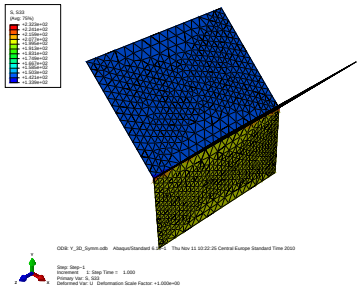

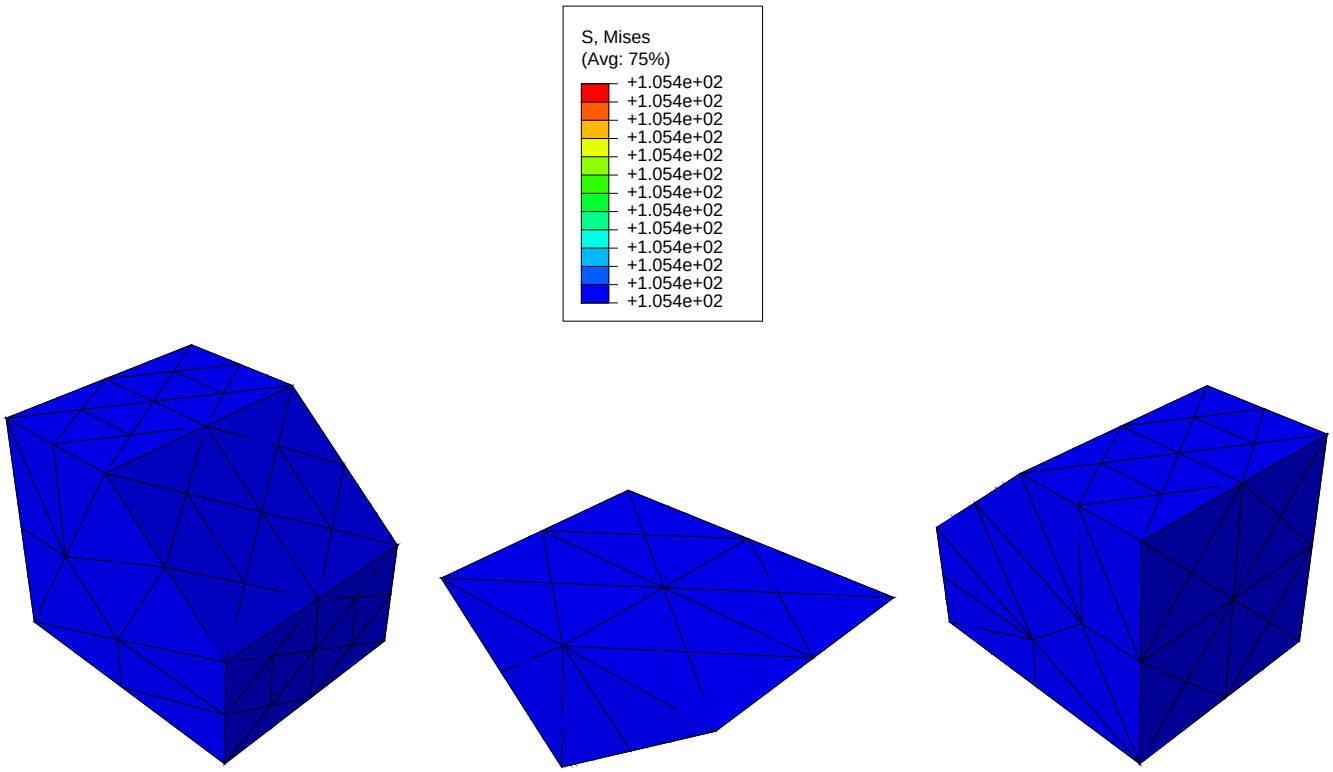

Figure 3.7: Mises stresses in individual grains with superimposed structural meshes.

In this section we ascertain the deviations for several additional combinations of structural and cohesive elements. First, Fig. 3.7 shows the Mises stresses for the grains. These are equal to the theoretically expected values from the stress tensor, Eq. (3.8). The non-conformal mesh had no influence on the computed Mises stresses. Second, the normal stresses on the grain boundary between the grain 1 and 2 are presented in Fig. 3.8 and Tables 3.6 through 3.8.

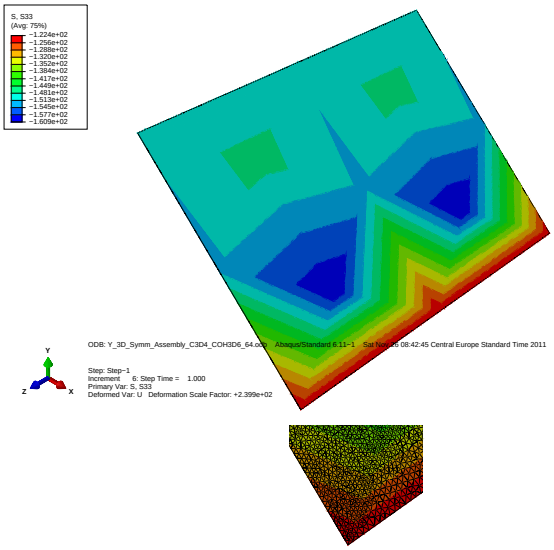

Structural: C3D4. Cohesive: COH3D6.

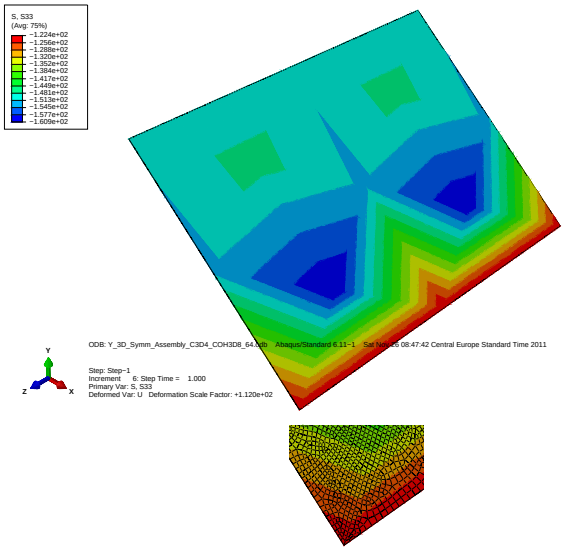

Structural: C3D4. Cohesive: COH3D8.

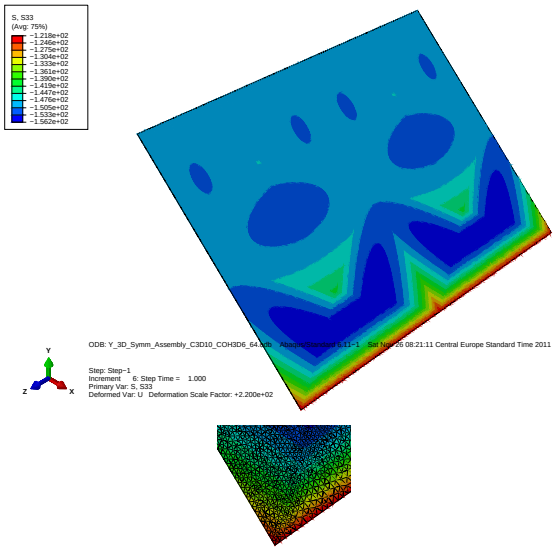

Structural: C3D10. Cohesive: COH3D6.

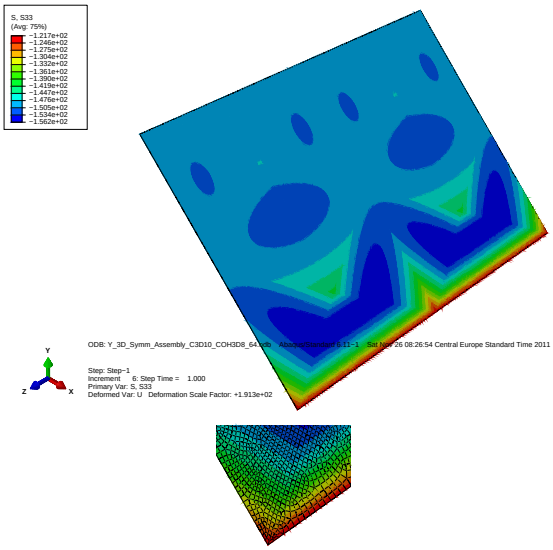

Structural: C3D10. Cohesive: COH3D8.

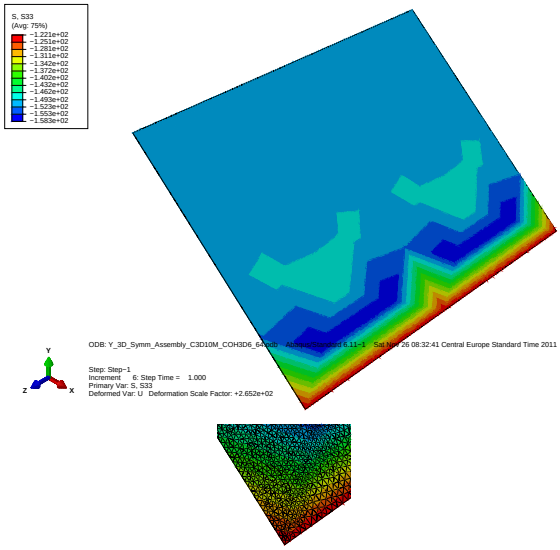

Structural: C3D10M. Cohesive: COH3D6.

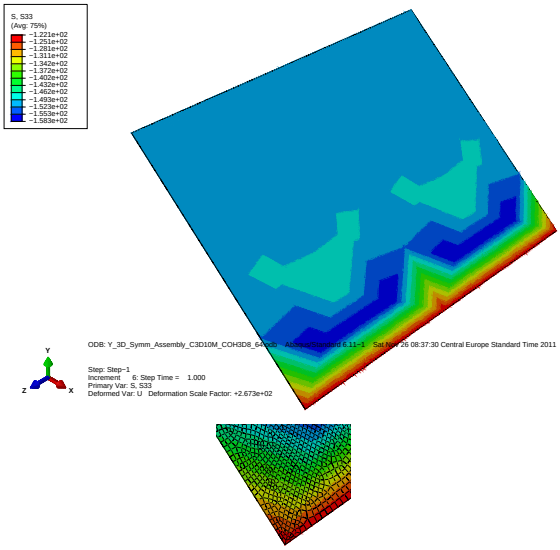

Structural: C3D10M. Cohesive: COH3D8.

Figure 3.8: Normal stresses on the grain boundary between grains 1 and 2. Theoretical normal stress value is 150 MPa. The inserts show the mesh densities with 64 elements per edge seeding. **NON-CONFORMAL MESHES**.

One has to bare in mind that the negative sign of the normal stresses is due to the different orientation of the normal. One can see that at the triple lines between the grains the normal stress is:

1. $Grain_1$ and $Grain_2$: underestimated by ≈30 % no matter which combination of structural and cohesive elements is used.
2. $Grain_2$ and $Grain_3$: underestimated by ≈30 % no matter which combination of structural and cohesive elements is used.
3. $Grain_1$ and $Grain_3$: overestimated by ≈25 % no matter which combination of structural and cohesive elements is used.

The effect of different combination of structural and cohesive elements is therefore quite small.

Element types	Computed normal stresses [MPa]	
	Minimal	Maximal
C3D4, COH3D6	-160.9	-122.4
C3D4, COH3D8	-160.9	-122.4
C3D10, COH3D6	-156.2	-121.8
C3D10, COH3D8	-156.2	-121.7
C3D10M, COH3D6	-158.3	-122.1
C3D10M, COH3D8	-158.3	-122.1

Table 3.6: Comparison of extreme normal stresses for different element types. Grain boundary between a) the $Grain_1$ and $Grain_2$ and b) the $Grain_2$ and $Grain_3$. Theoretical value is 150 MPa.

Element types	Computed normal stresses [MPa]	
	Minimal	Maximal
C3D4, COH3D6	-255.2	-178.1
C3D4, COH3D8	-255.2	-178.1
C3D10, COH3D6	-253.7	-188.3
C3D10, COH3D8	-253.7	-188.4
C3D10M, COH3D6	-255.0	-184.1
C3D10M, COH3D8	-255.1	-184.1

Table 3.7: Comparison of extreme normal stresses for different element types. Grain boundary between the $Grain_1$ and $Grain_3$. Theoretical value is 200 MPa.

Table 3.8 compares the extreme normal stress values for increasing mesh densities. One can see that the effect of the increased mesh densities has quite small effect on the computed extreme values of the normal stresses which still significantly deviate from the theoretical values.

Coh. el. per edge	Computed normal stresses [MPa] C3D4, COH3D6				Computed normal stresses [MPa] C3D10M, COH3D8			
	$Grain_1$-$Grain_2$		$Grain_1$-$Grain_3$		$Grain_1$-$Grain_2$		$Grain_1$-$Grain_3$	
	Minimal	Maximal	Minimal	Maximal	Minimal	Maximal	Minimal	Maximal
2	-154.0	-127.9	-244.1	-192.1	-163.4	-121.9	-243.2	-169.8
4	-158.4	-123.6	-248.2	-188.6	-172.6	-107.0	-235.0	-157.4
16	-160.7	-122.5	-254.6	-179.0	-160.5	-118.3	-251.7	-189.3
32	-160.9	-122.4	-255.1	-178.3	-158.7	-121.3	-254.1	-185.1
64	-160.9	-122.4	-255.2	-178.1	-158.3	-122.1	-255.1	-184.1

Table 3.8: Comparison of extreme normal stresses for different mesh densities and element types. Grain boundary between the $Grain_1$ and $Grain_2$: theoretical value is 150 MPa. Grain boundary between the $Grain_1$ and $Grain_3$: theoretical value is 200 MPa.

3.1.2 3D Voronoi tessellation

Fig. 3.9 shows a FE model of a structure containing 100 grains. The grain structure is obtained using 3D Voronoi tessellation through Qhull algorithm [18] and implemented in [19]. Fig. 3.10 displays the computed versus the theoretical normal stresses for the cohesive elements at external load of 70 MPa. Isotropic elastic constitutive law is used. The solid line represents the ideal response. One can observe a significant scatter from the ideal response. Fig. 3.11 displays the cohesive elements with red color indicating elements with more than 50 % difference between the theoretical and computed normal stresses. Also here one can observe that a significant scatter exists. Similar scatter has also been reported in the literature [20].

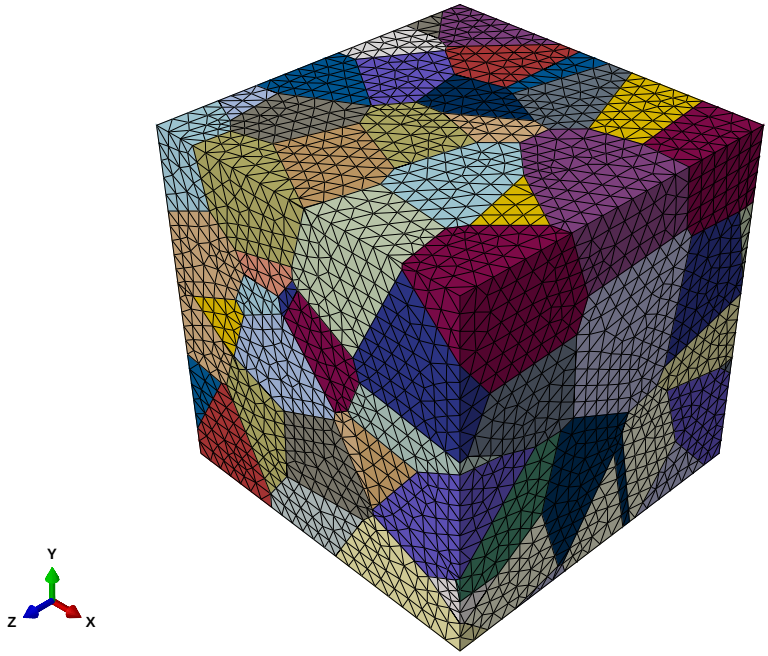

Figure 3.9: FE model of a structure with 100 grains obtained using 3D Voronoi tessellation.

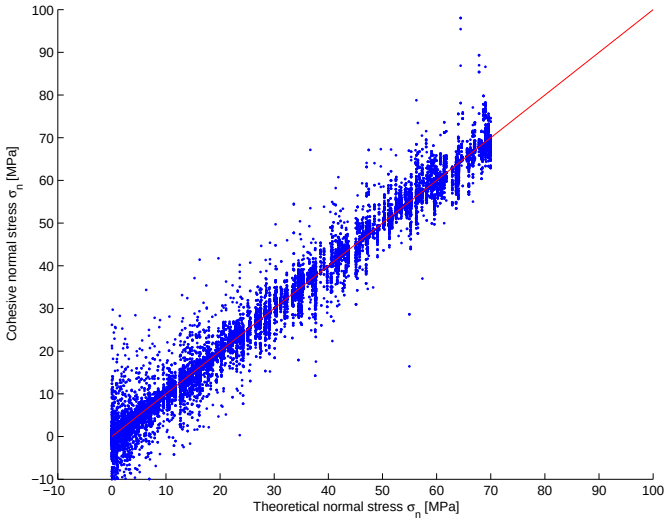

Figure 3.10: Theoretical and computed normal stresses at integration points of the cohesive elements [11]. Element size=0.025.

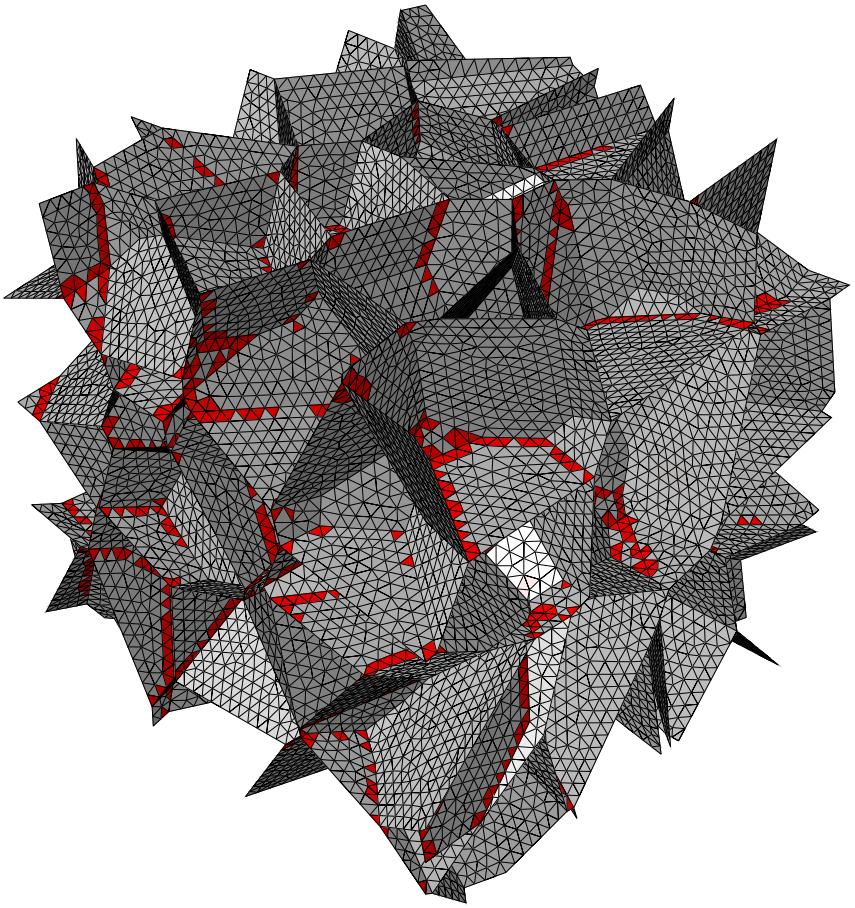

Figure 3.11: Cohesive elements with more than 50 % difference between the theoretical and computed normal stresses (in red) [11]. Element size=0.025.

3.1.3 As-measured grain structure

Fig. 3.12 shows a FE model of a 400 μm diameter stainless steel wire characterized in 3D by DCT [21]. The data has been kindly provided by the University of Manchester, Materials Performance Centre, School of Materials and comprises of 362 grains and some 1600 grain boundaries. Isotropic elastic constitutive law is used for the grains with the wire loaded in tension by applying tensile axial load of 60 MPa.

Fig. 3.13 displays the computed versus the theoretical normal stresses for the cohesive elements. The solid line represents the ideal response, the dashed lines indicate $\pm$20 % deviations. Vast majority of the problematic cohesive elements are located on the triple lines between the grains. The scatter of the normal stresses of the cohesive elements not lying on the triple lines is significantly smaller, with most values within the $\pm$20 % deviation. Increasing mesh density helps to alleviate the issue to some degree by reducing the area of the problematic elements. Other factors such as the stiffness of the cohesive element and its thickness have negligible effect on the scatter [10]. Fig. 3.14 displays the cohesive elements with red color indicating elements with more than 50 % difference between the theoretical and computed normal stresses.

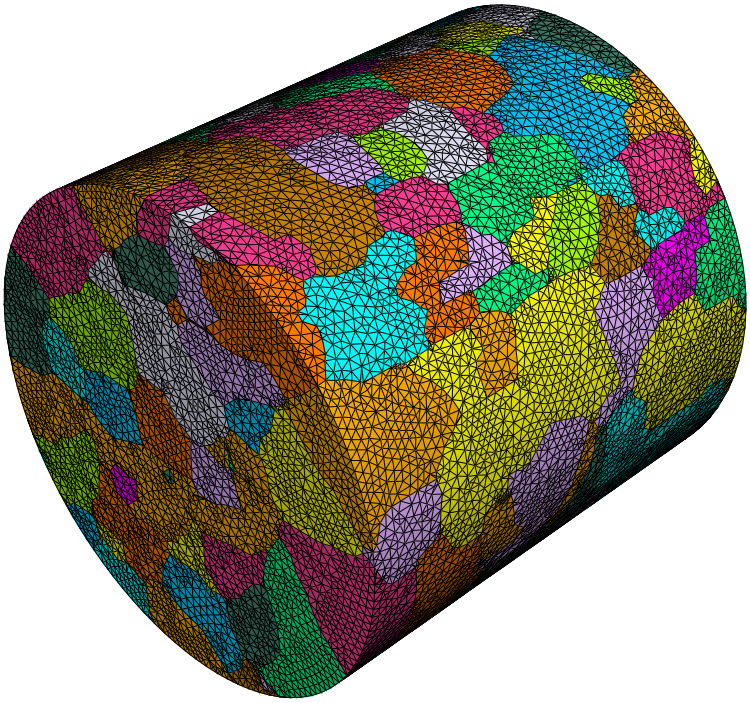

Figure 3.12: A FE model of the 400 μm diameter stainless steel wire, containing 362 grains.

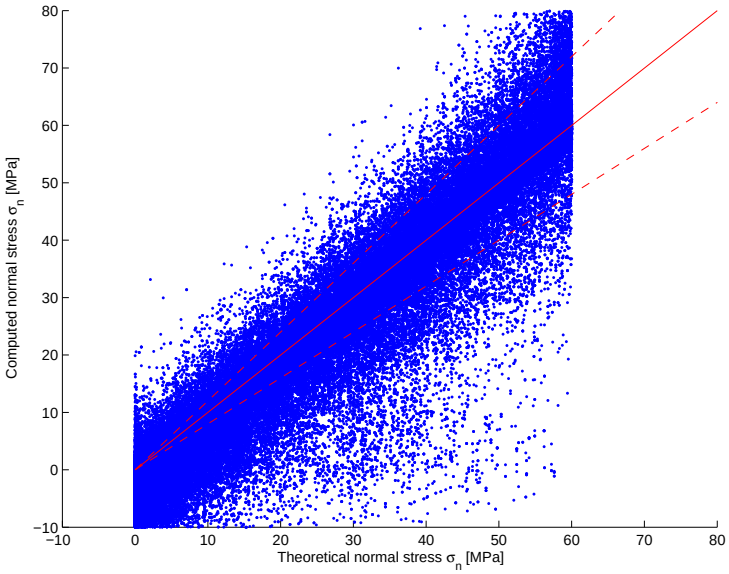

Figure 3.13: Theoretical and computed normal stresses at integration points of the cohesive elements [10]. Element size 10.0 μm. Solid line: theoretical response. Dashed lines: $\pm$20 % deviations.

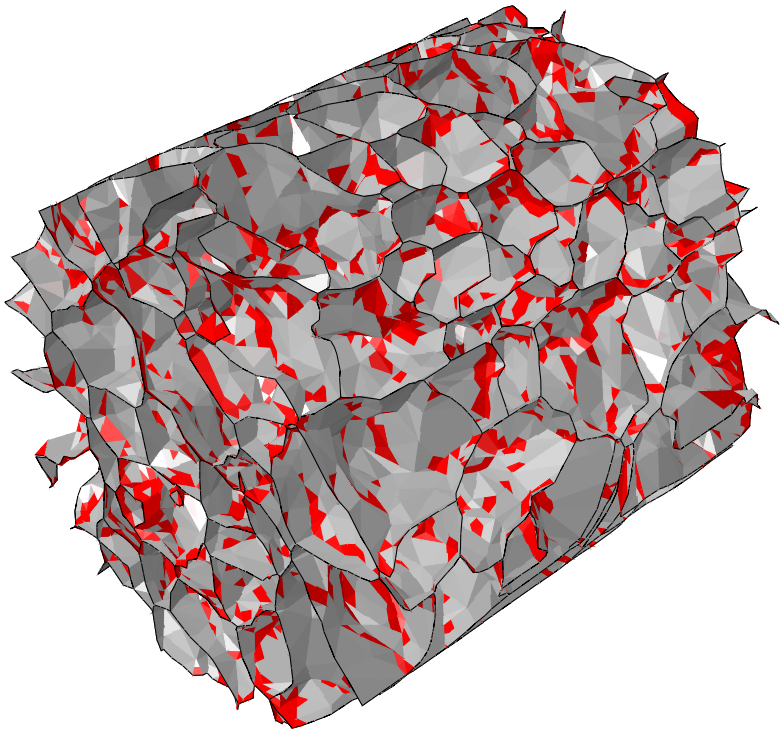

Figure 3.14: Grain boundaries with problematic cohesive elements highlighted in red [10]. Element size 10.0 μm.

Chapter 4

Conclusion

This work highlights some of the issues regarding the application of the cohesive elements for modeling grain boundaries with the purpose of capturing intergranular stress corrosion cracking in polycrystalline aggregates. The main issue relates to the computation of the normal stresses which at the triple lines between the grain boundaries deviate from the theoretically computed values for a homogeneous, isotropic material. The issues is found in both 3D type cohesive elements in ABAQUS: COH3D6 and COH3D8. Both conformal and non-conformal meshes were investigated and the issues is observed in both. Also, the effect of different structural elements and different mesh densities was investigated. Quite small influence of both was found. The only instance where the computed normal stresses agree well with the theoretical is in the case of a very simple geometry with a conformal and completely symmetric mesh. This kind of mesh is practically impossible to obtain in the real steel structure. The applicability of the cohesive elements in this type of application is therefore questionable.

Bibliography

[1] International Atomic Energy Agency. Assessment and Management of Ageing of Major Nuclear Power Plant Components Important to Safety: PWR Vessel Internals. Technical report, International Atomic Energy Agency, 2007.

[2] International Atomic Energy Agency. Heavy Component Replacement in Nuclear Power Plants: Experience and Guidelines. Technical report, International Atomic Energy Agency, 2008.

[3] U.S.NRC. Davis-Besse Reactor Pressure Vessel Head Degradation. Overview, Lessons Learned, and NRC Actions Based on Lessons Learned. Technical report, U.S.NRC, August 2008.

[4] B.C. Larson, W. Yang, G.E. Ice, J.D. Budai, and J.Z. Tischler. Three-dimensional X-ray structural microscopy with submicrometre resolution (http://dx.doi.org/10.1038/415887a). *Nature*, 415:887–890, February 2002.

[5] H. F. Poulsen. *Three-Dimensional X-Ray Diffraction Microscopy: Mapping Polycrystals and their Dynamics*. Springer, 1st edition, October 2004.

[6] W. Ludwig, S. Schmidt, E. M. Lauridsen, and H. F. Poulsen. X-ray diffraction contrast tomography: a novel technique for three-dimensional grain mapping of polycrystals. I. Direct beam case (http://dx.doi.org/10.1107/s0021889808001684). *Journal of Applied Crystallography*, 41(2):302–309, April 2008.

[7] G. Johnson, A. King, M. G. Honnicke, J. Marrow, and W. Ludwig. X-ray diffraction contrast tomography: a novel technique for three-dimensional grain mapping of polycrystals. II. The combined case (http://dx.doi.org/10.1107/s0021889808001726). *Journal of Applied Crystallography*, 41(2):310–318, April 2008.

[8] M. Herbig, P. King, A.and Reischig, H. Proudhon, E. M. Lauridsen, J. Marrow, J-Y Buffire, and W. Ludwig. 3-D growth of a short fatigue crack within a polycrystalline microstructure studied using combined diffraction and phase-contrast X-ray tomography. *Acta Materialia*, 59(2):590–601, January 2011.

[9] I. Simonovski and L. Cizelj. Computational multiscale modeling of intergranular cracking (http://dx.doi.org/10.1016/j.jnucmat.2011.03.051). *Journal of Nuclear Materials*, 44(22):243–250, July 2011.

[10] I. Simonovski and L. Cizelj. Towards Modeling Intergranular Stress Corrosion Cracks on Grain Size Scales (in presss). *Nuclear Engineering and Design*, 2011.

[11] Dr. Zakhariev, editor. *Polycrystalline Materials - Theoretical and Practical aspects*. INTECH, 2011.

[12] V.R. Coffman and J.P. Sethna. Grain boundary energies and cohesive strength as a function of geometry (http://link.aps.org/doi/10.1103/physrevb.77.144111). *Physical review B*, 77(14):1–11, April 2008.

[13] P. P. Camanho and C. G. Davila. Mixed-mode decohesion finite elements for the simulation of delamination in composite materials. Technical report, NASA, 2002.

[14] Simulia. *ABAQUS 6.10-1 (http://www.simulia.com/)*, 2010.

[15] J.F. Molinari, G. Gazonas, R. Raghupathy, A. Rusinek, and F. Zhou. The cohesive element approach to dynamic fragmentation: The question of energy convergence. *International Journal for Numerical Methods in Engineering*, 69:484–503, 2007.

[16] R. Schapery. A theory of crack initiation and growth in viscoelastic media I. Theoretical development (http://dx.doi.org/10.1007/bf00034721). *International Journal of Fracture*, 11(1):141–159, February 1975.

[17] A.C. Palmer and J.R. Rice. The growth of slip surfaces in the progressive failure of over-consolidated clay. *Proceedings of the Royal Society of London, Series A*, 332:527–548, 1973.

[18] Qhull code for convex hull, delaunay triangulation, voronoi diagram, and halfspace intersection about a point. http://www.qhull.org.

[19] Z. Petrič. Generating 3D Voronoi tessellations for material modeling. Technical report, Jozef Stefan Institute, 2010.

[20] M. Kamaya and M. Itakura. Simulation for intergranular stress corrosion cracking based on a three-dimensional polycrystalline model. *Engineering Fracture Mechanics*, 76(3):386–401, February 2009.

[21] A. King, G. Johnson, D. Engelberg, W. Ludwig, and J. Marrow. Observations of Intergranular Stress Corrosion Cracking in a Grain-Mapped Polycrystal (http://dx.doi.org/10.1126/science.1156211, http://www.sciencemag.org/cgi/content/full/321/5887/382). *Science*, 321(5887):382 – 385, July 2008.

Index

European Commission

EUR 25144 EN - Joint Research Centre - Institute for Energy and Transport
Title: Grain boundary modeling issues with cohesive elements: application to intergranular stress corrosion cracking.
Author(s): Igor Simonovski, Gangadhar Machina
Luxembourg: Publications Office of the European Union
2012 - 30 pp. - 21 x 29.7 cm
EUR - Scientific and Technical Research series - ISSN 1831-9424 (online), ISSN 1018-5593 (print)
ISBN 978-92-79-22608-3(pdf)
ISBN 978-92-79-22607-6(print)
doi http://dx.doi.org/10.2790/40327

Abstract
This work highlights some of the issues regarding the application of the cohesive elements for modeling grain boundaries with the purpose of capturing intergranular stress corrosion cracking in polycrystalline aggregates. The main issue relates to the computation of the normal stresses which at the triple lines between the grain boundaries deviate from the theoretically computed values for a homogeneous, isotropic material. The issues is found in both 3D type cohesive elements in ABAQUS: COH3D6 and COH3D8. Both conformal and non-conformal meshes were investigated and the issues is observed in both. Also, the effect of different structural elements and different mesh densities was investigated. Quite small influence of both was found. The only instance where the computed normal stresses agree well with the theoretical is in the case of a very simple geometry with a conformal and completely symmetric mesh. This kind of mesh is practically impossible to obtain in the real steel structure. The applicability of the cohesive elements in this type of application is therefore questionable.

The mission of the Joint Research Centre is to provide customer-driven scientific and technical support for the conception, development, implementation and monitoring of EU policies. As a service of the European Commission, the JRC functions as a reference centre of science and technology for the Union. Close to the policy-making process, it serves the common interest of the Member States, while being independent of special interests, whether private or national.

JRC
EUROPEAN COMMISSION

LD-NA-25144-EN-N

Publications Office

ISBN 978-92-79-22608-3